Nematohydrodynamics for Colloidal Self-Assembly and Transport Phenomena

Sourav Mondal[a], Apala Majumdar[b], Ian M. Griffiths[a,*]

[a]*Mathematical Institute, University of Oxford, Oxford OX2 6GG, UK*
[b]*Department of Mathematical Sciences, University of Bath, Bath BA2 7AY, UK*

Abstract

Hypothesis

Colloidal particles in a nematic liquid crystal (NLC) exhibit very different behaviour than that observed in an isotropic medium. Such differences arise principally due to the nematic-induced elastic stresses exerted as due to the interaction of NLC molecules with interfaces, which competes with traditional fluid viscous stresses on the particle.

Theory

A systematic mathematical analysis of the behaviour of particles placed in the flow within an NLC microfluidic channel is performed using the continuum Beris–Edwards framework coupled to the Navier–Stokes equations. We impose strong homeotropic anchoring on the channel walls and weak homeotropic anchoring on the particle surfaces.

Findings

The viscous and NLC forces act on an individual particle in opposing directions, resulting in a critical location in the channel where the particle experiences zero net force in the direction perpendicular to the flow. For multi-particle aggregation we show that the final arrangement is independent of the initial configuration, but the path towards achieving equilibrium is very different. The results of our work uncover new mechanisms for particle separation and routes towards self-assembly.

Keywords: nematic fluid, microchannel, Beris–Edwards, particle dynamics

1. Introduction

Nematic liquid crystals (NLCs) are important examples of complex anisotropic fluids with locally preferred directions [1]. NLCs combine the intrinsic fluidity of liquids with

∗Corresponding author
Email address: ian.griffiths@maths.ox.ac.uk (Ian M. Griffiths)

long-range orientational ordering of the constituent rod-like molecules. The orientational order couples with the flow and induces novel effects compared with isotropic Newtonian fluids, such as backflow, anisotropic stresses and multiple viscosities. The study of NLCs in microfluidic environments is relatively new, with substantial experimental interest since around 2011. Subsequently, experimentalists have highlighted the immense potential of NLC microfluidics for transport, mixing and particle separation [2, 3], while the ability of NLCs to spontaneously organize micron-size particles into regular patterns shows great promise [4]. For example, it is possible to generate defect or disclination lines in an NLC microfluidic set-up with an appropriate choice of boundary conditions, material parameters, temperature and flow effects and these defect lines can naturally attract colloidal particles or micro-cargo, which are subsequently transported along these lines as self-assembled chains [3, 5]. Further, the forces facilitating spatial-reorganization of colloidal dispersions in an NLC medium are two to three orders of magnitude higher than in water-based colloids [6, 7].

In the bulk NLC, additional long-range interactions between particles are present because of the competition between elasticity and the interaction between NLC molecules and surfaces (termed 'anchoring'), implying that colloids suspended in a nematic matrix are qualitatively different from their isotropic analogues. The particle sets a certain director distortion around itself, due to the surface anchoring conditions; the director distortions lead to long-range elastic interactions of the particle with the bounding walls (or neighbouring interfaces); and the nematic order leads to an anisotropy in the Stokes drag [8, 9]. These features mean that rich self-ordering phenomena can be observed, which is characterized by strong interplay between the colloidal size, NLC anisotropies, particle and surface anchoring properties [3, 10, 11, 12].

There is a wealth of literature on nematohydrodynamics in the absence of particle inclusions [13, 14]. The analysis of the impact of placing a particle in an NLC has generally been focused on how the NLC reorders around a single particle that is held in position [15] or the transitions in the flow profiles [16, 17]. More recent experimental studies have focused on the dynamic behaviour of (finite sized) suspended colloidal particles in a nematic-fluid flow [1, 3, 7, 18].

Our work is motivated by the experiments conducted by Sengupta et al. in [2]. Here the authors study an NLC microfluidic set-up experimentally and numerically in three

different flow regimes: weak, medium and strong, and report on both the flow profiles and the averaged local molecular alignment profiles, referred to as "director" profiles in the continuum-modelling literature. The surfaces of the microfluidic channel are treated to induce homeotropic boundary conditions, so that the nematic molecules are preferentially anchored along the normal to the boundary surfaces, or equivalently the continuum "director" is parallel to the normal to the channel walls. A flow is induced by applying a pressure gradient at the inlet and the observations seem to be invariant across the width of the cell.

In this paper we focus on three separate aspects: (i) a static particle at the centre with variable anchoring strength on its boundary, (ii) the forces experienced by a particle inclusion due to hydrodynamic effects, nematic stresses and attractive forces induced by the boundary conditions and (iii) the dynamics of two and three particles in an NLC microfluidic environment including the transient dynamics.

We mathematically model the NLC microfluidic environment using the nematodynamics formulation used in [19]. The state of nematic alignment is described by a two-dimensional (2D) Landau-de Gennes (LdG) $\mathbf{Q}$-tensor, which is a symmetric traceless two-by-two matrix with two degrees of freedom: an angle θ that describes the preferred in-plane alignment of the nematic molecules or the direction of the nematic director $\boldsymbol{n}$, and a scalar order parameter, s, that is a measure of the degree of alignment about the director $\boldsymbol{n}$. We investigate how the particles interact with the NLC environment in the absence and presence of flow, for both static and moving particles. The first example concerns a static particle in the NLC microfluidic cell with no fluid flow. For a given anchoring strength on the particle boundary, we study the director profile around the particle as a function of its size and, for a given particle size, we investigate the surrounding director profile as a function of anchoring strength. In both cases, there is a narrow window of parameters within which the director orientation on the particle boundary switches from uniform to normal/homeotropic and we numerically explore the switch in different cases. We then systematically study the force experienced by the particle including the effects of a flow field, particle surface anchoring, and the particle size. In particular, for a given anchoring strength and flow velocity, there is a critical particle size (relative to the channel dimensions) such that, in contrast to conventional liquids, the force attains a maximum, decreasing for larger particles owing to the attractive forces exerted by the boundaries.

We conclude by studying the motion of two and three colloidal particles in the microfluidic channel, including the transient re-alignment dynamics, how the particles get attracted to each other starting from different initial configurations and are transported through the channel as an agglomerate.

2. Theory

We consider a two-dimensional NLC microfluidic channel (parallel-plate geometry) as shown in Fig. 1. The nematic director $\boldsymbol{n} = (\cos\theta, \sin\theta)$, represents the locally preferred in-plane alignment of the NLC molecules relative to the horizontal axis. We consider a circular particle, whose boundary is parameterized by the angle ϕ to the horizontal axis. We apply strong homeotropic anchoring conditions on the channel walls (modelled by Dirichlet conditions) while the anchoring conditions on the colloidal particle are varied from weak to strong in terms of an anchoring coefficient. Provided the channel dimension into the page (z direction) is large compared with the channel height (in the y direction, i.e., $2L_2$ in Fig. 1) then this two dimensional approximation is valid [20, 21]. We note that the three-dimensional analogue of this two-dimensional set-up would in principle correspond to cylindrical particles. However, similar methods can be applied to studied to spherical colloidal particles in an NLC microfluidic channel, though this requires further study. When these dimensions are comparable then the problem is fully three dimensional, as seen in [22, 23]. Whilst we do not consider this scenario in this paper, we analyse this further in Appendix A of the Supplementary Information. The fluid flow in the device is driven by an external pressure difference and by the nematic ordering. We impose no-slip conditions on the channel walls and particle surface.

The flow hydrodynamics are described by the incompressible Navier–Stokes equations with an additional stress ($\boldsymbol{\sigma}$) due to the NLC orientational ordering [19, 24],

$$\nabla \cdot \boldsymbol{u} = 0, \tag{1}$$

$$\rho\left(\frac{\partial \boldsymbol{u}}{\partial t} + \boldsymbol{u}\cdot\nabla\boldsymbol{u}\right) = -\nabla p + \nabla\cdot(\mu[\nabla\boldsymbol{u} + (\nabla\boldsymbol{u})'] + \boldsymbol{\sigma}). \tag{2}$$

Here $\nabla = \left(\frac{\partial}{\partial x}, \frac{\partial}{\partial y}\right)$, ρ and μ are the density and viscosity of the fluid medium respectively, p is the hydrodynamic pressure, $\boldsymbol{u}$ is the fluid velocity and $\mu[\nabla\boldsymbol{u} + (\nabla\boldsymbol{u})']$ is the viscous stress experienced by the fluid ($[\nabla\boldsymbol{u}]'$ is the transpose of $\nabla\boldsymbol{u}$). The NLC stress ($\boldsymbol{\sigma}$) is

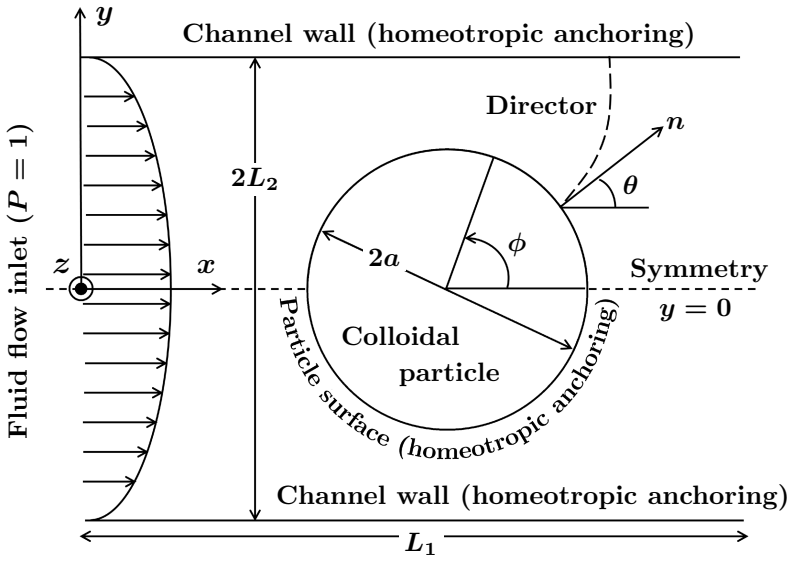

Figure 1: Schematic of the problem definition and system geometry showing the reference co-ordinate system. The fluid flow is in the direction of positive x.

given by [19, 13, 25, 26, 2],

$$\boldsymbol{\sigma} = -\lambda s\boldsymbol{h} + \boldsymbol{q}\boldsymbol{h} - \boldsymbol{h}\boldsymbol{q}, \tag{3}$$

where $s = \sqrt{2}|\boldsymbol{q}|$ is the scalar order parameter and $\boldsymbol{h}$ is the molecular field, which controls the relaxation to equilibrium and is given by

$$\boldsymbol{h} = \kappa\nabla^2\boldsymbol{q} - A\boldsymbol{q} - C|\boldsymbol{q}|^2\boldsymbol{q}. \tag{4}$$

Here, $\boldsymbol{q}$ is the nematic order parameter, a symmetric and traceless 2×2 matrix, used to describe the NLC state and is referred to as the two-dimensional LdG tensor [27],

$$\boldsymbol{q} = \begin{pmatrix} q_{11} & q_{12} \\ q_{12} & -q_{11} \end{pmatrix}; \tag{5}$$

κ is the NLC elastic constant, A and C are material and temperature-dependent coefficients and λ is the (dimensionless) NLC alignment parameter, which reflects whether the NLC response is affected by the fluid strain or vorticity and is determined experimentally [25, 28, 29].

The tensor $\boldsymbol{q}$ and the director $\boldsymbol{n}$ are related by $\boldsymbol{q} = s\,(\boldsymbol{n} \otimes \boldsymbol{n} - \mathbf{I}/2)$ where $\mathbf{I}$ is the identity matrix in 2D and $s^2 = 2|\boldsymbol{q}|^2$. We recover the director angle from the relation $\theta = \frac{1}{2}\tan^{-1}(q_{12}/q_{11})$. In [19], the evolution equation for $\boldsymbol{q}$ is given by [30, 19, 24]

$$\frac{\partial \boldsymbol{q}}{\partial t} + \boldsymbol{u}\cdot\nabla\boldsymbol{q} = \frac{1}{2}\lambda s[\nabla\boldsymbol{u} + (\nabla\boldsymbol{u})'] + \boldsymbol{q}\boldsymbol{\omega} - \boldsymbol{\omega}\boldsymbol{q} + \frac{1}{\Gamma}\boldsymbol{h}, \tag{6}$$

where Γ is the rotational diffusion coefficient [25] and $\boldsymbol{\omega} = \nabla \times \boldsymbol{u}$ is the anti-symmetric part of the velocity gradient tensor, or vorticity tensor. We label $\boldsymbol{q}$ as a 2D vector with two independent components, $\boldsymbol{q} = (q_{11}, q_{12})$ where $q_{11} = \frac{s}{2}\cos 2\theta$ and $q_{12} = \frac{s}{2}\sin 2\theta$. We impose strong homeotropic conditions on the channel walls so that

$$\boldsymbol{q} = \left(\frac{2|A|}{C}\right)^{1/2}\left(\boldsymbol{\nu}_{\pm} \otimes \boldsymbol{\nu}_{\pm} - \frac{\boldsymbol{I}}{2}\right), \tag{7}$$

where $\boldsymbol{\nu}_{\pm} = (0, \pm 1)$ are the unit outward normals at the channel walls $y = \pm L_2$, where L_2 is the channel half height as depicted in Fig. 1.

On the particle, we apply a mixed anchoring condition,

$$-\kappa \nabla q_{11} \cdot \boldsymbol{\nu}_p = w\left(q_{11} + \sqrt{\frac{A}{2C}}\right), \tag{8a}$$

$$-\kappa \nabla q_{12} \cdot \boldsymbol{\nu}_p = w q_{12}, \tag{8b}$$

where $\boldsymbol{\nu}_p$ is the unit normal to the particle surface and w is an anchoring-strength parameter. When $w = 0$, (8) reduces to Neumann boundary conditions and $w \to \infty$ is the Dirichlet strong homeotropic anchoring limit.

2.1. Non-dimensionalization

We non-dimensionalize equations (1)–(6) by applying the following scalings:

$$\begin{aligned} X &= \frac{x}{L_2}, & Y &= \frac{y}{L_2}, & U &= \frac{u}{u_0}, \\ V &= \frac{v}{u_0}, & P &= \frac{pL_2}{\mu u_0}, & T &= \frac{u_0 t}{L_2}, \end{aligned} \tag{9}$$

where u_0 is the mean channel velocity and μ is the fluid viscosity. The dimensionless versions of Eqs. (1)–(4) are then

$$\frac{\partial U}{\partial X} + \frac{\partial V}{\partial Y} = 0, \tag{10}$$

$$\begin{aligned} Re\left(\frac{\partial U}{\partial T} + U\frac{\partial U}{\partial X} + V\frac{\partial U}{\partial Y}\right) &= -\frac{\partial P}{\partial X} + \frac{\partial^2 U}{\partial X^2} + \frac{\partial^2 U}{\partial Y^2} \\ &+ \frac{1}{Er}\frac{|A^*|}{2C^*}\frac{\partial}{\partial X}(-\lambda S H_{11}) + \frac{1}{Er}\frac{|A^*|}{2C^*}\frac{\partial}{\partial Y}(-\lambda S H_{12} - \eta), \end{aligned} \tag{11}$$

$$\begin{aligned} Re\left(\frac{\partial V}{\partial T} + U\frac{\partial V}{\partial X} + V\frac{\partial V}{\partial Y}\right) &= -\frac{\partial P}{\partial Y} + \frac{\partial^2 V}{\partial X^2} + \frac{\partial^2 V}{\partial Y^2} \\ &+ \frac{1}{Er}\frac{|A^*|}{2C^*}\frac{\partial}{\partial X}(-\lambda S H_{12} + \eta) + \frac{1}{Er}\frac{|A^*|}{2C^*}\frac{\partial}{\partial Y}(\lambda S H_{11}). \end{aligned} \tag{12}$$

Here $\boldsymbol{H}$ is the dimensionless molecular field given by

$$\boldsymbol{H} = \frac{\partial^2 \boldsymbol{Q}}{\partial X^2} + \frac{\partial^2 \boldsymbol{Q}}{\partial Y^2} - A^* \left(1 + \frac{1}{4} S^2\right) \boldsymbol{Q}, \tag{13}$$

where

$$A^* = \frac{A L_2^2}{\kappa}, \qquad C^* = \frac{C L_2^2}{\kappa}, \qquad \boldsymbol{H} = \boldsymbol{h} \frac{L_2^2}{\kappa} \sqrt{\frac{2C^*}{|A^*|}},$$
$$\boldsymbol{Q} = \boldsymbol{q} \sqrt{\frac{2C^*}{|A^*|}}, \qquad \eta = 2(Q_{12} H_{11} - Q_{11} H_{12}), \qquad S = s \sqrt{\frac{2C^*}{|A^*|}}; \tag{14}$$

$Er = u_0 \mu L_2 / \kappa$ denotes the Ericksen number, the ratio of the viscous to NLC elastic forces and $Re = \rho u_0 L_2 / \mu$ is the Reynolds number, which quantifies the relative magnitude of the inertial to viscous forces. In microfluidic flows, $Re \ll 1$ (Table 1 gives typical operating regimes $10^{-6} < Re < 10^{-3}$), which reduces Eqs. (11)–(12) to a Stokes flow (where the inertial terms on the left-hand side are ignored), so that

$$\frac{\partial P}{\partial X} = \frac{\partial^2 U}{\partial X^2} + \frac{\partial^2 U}{\partial Y^2} + \frac{1}{Er} \frac{|A^*|}{2C^*} \frac{\partial}{\partial X}(-\lambda S H_{11}) + \frac{1}{Er} \frac{|A^*|}{2C^*} \frac{\partial}{\partial Y}(-\lambda S H_{12} - \eta), \tag{15}$$

$$\frac{\partial P}{\partial Y} = \frac{\partial^2 V}{\partial X^2} + \frac{\partial^2 V}{\partial Y^2} + \frac{1}{Er} \frac{|A^*|}{2C^*} \frac{\partial}{\partial X}(-\lambda S H_{12} + \eta) + \frac{1}{Er} \frac{|A^*|}{2C^*} \frac{\partial}{\partial Y}(\lambda S H_{11}). \tag{16}$$

For the flow problem, we apply the following boundary conditions: no slip and no penetration on the channel walls and particle surface,

$$U = 0, \qquad V = 0, \tag{17}$$

on $Y = \pm 1 \ \forall X$ and $X^2 + Y^2 = R^2$, where $R = r/L_2$ is the dimensionless radius of the colloidal particle and pressure boundary conditions at the channel entrance and exit,

$$P = 1 \qquad \text{on} \quad X = -L_1/2L_2, \qquad -1 \le Y \le 1, \tag{18}$$

$$P = 0 \qquad \text{on} \quad X = L_1/2L_2, \qquad -1 \le Y \le 1. \tag{19}$$

The dimensionless versions of the evolution equations (6) are

$$\frac{\partial Q_{11}}{\partial T} + U \frac{\partial Q_{11}}{\partial X} + V \frac{\partial Q_{11}}{\partial Y} = \lambda S \frac{\partial U}{\partial X} - Q_{12} \left(\frac{\partial V}{\partial X} - \frac{\partial U}{\partial Y}\right) + \frac{\mu/\Gamma}{Er} H_{11}, \tag{20}$$

$$\frac{\partial Q_{12}}{\partial T} + U \frac{\partial Q_{12}}{\partial X} + V \frac{\partial Q_{12}}{\partial Y} = \frac{1}{2} \lambda S \left(\frac{\partial V}{\partial X} + \frac{\partial U}{\partial Y}\right) - Q_{11} \left(\frac{\partial V}{\partial X} - \frac{\partial U}{\partial Y}\right) + \frac{\mu/\Gamma}{Er} H_{12}. \tag{21}$$

The strong homeotropic boundary conditions (7) translate to

$$Q_{11} = -1, \qquad Q_{12} = 0. \tag{22a,b}$$

The anchoring conditions on the particle, (8), become

$$-\tilde{\nabla}Q_{11}\cdot\boldsymbol{\nu}_p = W(Q_{11}+1), \tag{23a}$$

$$-\tilde{\nabla}Q_{12}\cdot\boldsymbol{\nu}_p = WQ_{12}, \tag{23b}$$

where $\tilde{\nabla} = (\partial/\partial X, \partial/\partial Y)$ is the dimensionless gradient operator, and $W = wL_2/\kappa$ is the dimensionless anchoring parameter.

2.2. Force exerted on the particle

The total dimensional force (per unit length), $\boldsymbol{f}$, on a particle of radius r in an NLC medium [31, 32, 33] is given by,

$$\boldsymbol{f} = \int_{\psi} (-p\boldsymbol{I} + \mu[\nabla\boldsymbol{u} + (\nabla\boldsymbol{u})'] + \boldsymbol{\sigma})\cdot\boldsymbol{\nu}_p \,\mathrm{d}\xi, \tag{24}$$

where ψ defines the circular boundary of the particle and $\boldsymbol{\nu}_p$ denotes the unit normal to the surface. The displacement of the particle can be calculated from the Stokes drag equation

$$\boldsymbol{f} = 3\pi\mu(\boldsymbol{u} - \dot{\boldsymbol{x_p}}), \tag{25}$$

where $\boldsymbol{x_p} = (x_p, y_p)$ denotes the instantaneous position of the particle centre and a dot represents differentiation with respect to time.

Non-dimensionalizing Eq. (24) via (9) and choosing the natural force scaling $\boldsymbol{F} = \boldsymbol{f}/\mu u_0$ gives the dimensionless drag (F_x) and lift (F_y) components of the force experienced by the particle (i.e., the forces in the x and y directions, respectively),

$$F_x = \int_{\Psi}\Bigg[\left(2\frac{\partial U}{\partial X} - P - \frac{1}{Er}\frac{|A^*|}{2C^*}\lambda S H_{11}\right)\nu_x + \left(\frac{\partial U}{\partial Y} + \frac{\partial V}{\partial X} - \frac{1}{Er}\frac{|A^*|}{2C^*}(\lambda S H_{12} + \eta)\right)\nu_y\Bigg]\mathrm{d}\Omega, \tag{26}$$

$$F_y = \int_{\Psi}\Bigg[\left(\frac{\partial U}{\partial Y} + \frac{\partial V}{\partial X} - \frac{1}{Er}\frac{|A^*|}{2C^*}(\lambda S H_{12} - \eta)\right)\nu_x + \left(2\frac{\partial V}{\partial Y} - P + \frac{1}{Er}\frac{|A^*|}{2C^*}\lambda S H_{11}\right)\nu_y\Bigg]\mathrm{d}\Omega, \tag{27}$$

where Ψ denotes the perimeter of the particle in the dimensionless domain and $\boldsymbol{\nu}_p = (\nu_x, \nu_y)$. The dimensionless version of Eq. (25) reads as

$$3\pi(U - \dot{X}_P) = F_x, \tag{28a}$$

$$3\pi(V - \dot{Y}_P) = F_y, \tag{28b}$$

where $\dot{X}_P = \mathrm{d}X_P/\mathrm{d}T$ and $\dot{Y}_P = \mathrm{d}Y_P/\mathrm{d}T$ are the respective dimensionless particle velocity components.

Table 1: Typical values of the physical parameters

Parameter [units]	Typical values [reference]
Elastic constant, κ $[pN]$	40 [2]
Length of the microchannel, L_1 $[\mu m]$	50
Half-height of the microchannel, L_2 $[\mu m]$	10
Particle radius, r $[\mu m]$	3
Mean fluid velocity, u_0 $[\mu m/s]$	10
Rotational diffusion constant, Γ $[Pa\,s]$	7.3 [2]
Viscosity, μ $[Pa\,s]$	0.01 [21]
NLC material property, A $[MJ/m^3]$	-0.172 [2]
NLC material property, C $[MJ/m^3]$	1.72 [2]
Dimensionless parameters used in calculation	
NLC alignment parameter, λ	1 [2]
Dimensionless particle radius, R	0.3
Reynolds number, Re	0.0001
Ericksen number, Er	0.01 – 100
Parameter, $\lvert A^*\rvert/C^*$	0.1
Relative anchoring strength, $\log W$	3

3. Results and Discussion

The coupled system of the equations (10–23) are solved numerically using a finite element software COMSOL v5.2 [34]. The details of the numerical techniques and the solver settings are given in the Supplementary Information (Section B).

3.1. Static particle and no fluid flow

We first compute the equilibrium director profiles and the order parameter S in the absence of a flow field $U = V = 0$ (or $Er = 0$). In this case we need only solve Eqs. (20) and (21), which reduce to $H_{11} = H_{12} = 0$ respectively, subject to the boundary conditions (22) and (23). We vary the anchoring strength parameter at the particle surface from weak to strong (homeotropic) anchoring (Fig. 2). There have been both experimental [35] and theoretical studies [36] where such ranges (over orders of magnitude) of the anchoring strength have been studied for physically realistic scenarios.

In [35] there are several surface anchoring values reported for different combinations of NLC materials and surfaces, which correspond to $\log W \approx 0 - 2$. In [36] the authors have studied the effect of surface anchoring strength (varying from $\log W \approx 1 - 2$) on the stability of the nematic ordering.

Surface anchoring strengths can be altered by photo-excitation [37], electric or magnetic fields [38, 39] or chemical surface functionalization [40]. Defects along the axial symmetry line ($Y = 0$) are observed, consistent with the literature reports [14, 41, 17, 42]. The contours of the order parameter are also qualitatively similar to the report of Fukuda et al. [13] and Sengupta et al. [43]. For low anchoring strengths, the defects are almost pinned to the particle surface, migrating away from the particle surface with increasing anchoring strength; at present there has been little experimental investigation along these lines.

The director field on the particle surface is very sensitive to the change in anchoring strength in the range $0.5 < \log W < 1$ for $R = 0.3$ (Fig. 3a). The anchoring switches from being effectively uniform (zero anchoring) to homeotropic (strong anchoring) within this range.

The effect of the particle size has a profound influence on the director field (Fig. 3b–d), particularly with increasing anchoring strength. As the particle size increases, the distance between the particle surface and channel walls reduces, inducing strong coupling between the directors on the particle surface and on the channel walls. Again there is a narrow range of R over which the director orientation switches from uniform to homeotropic on the particle boundary. The values of R in the transition region decrease with increasing $\log W$ (Fig. 3b–d). For example, in the case of $W = 3.2$ the transition occurs for $0.7 < R < 0.8$ (Fig. 3c), whereas for $W = 10$, the same occurs in the range

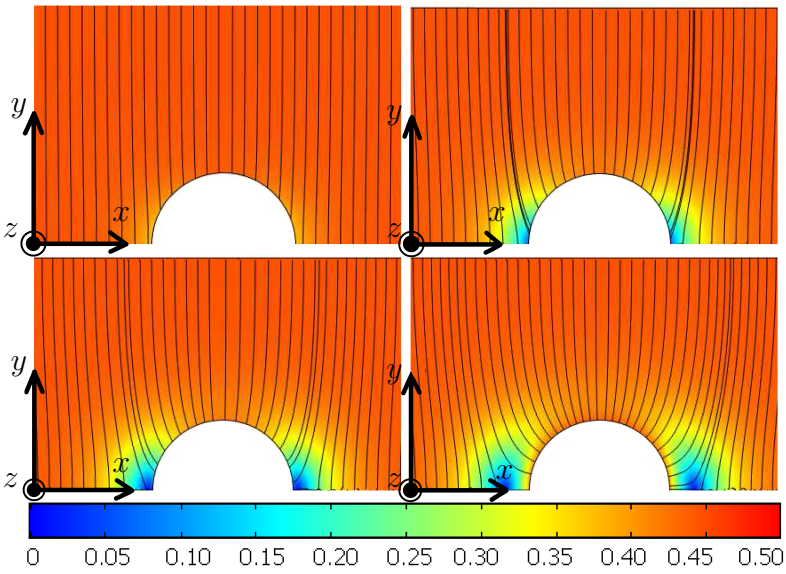

Figure 2: Orientation of the director field around the particle with homeotropic boundary conditions on the channel walls with zero flow field ($Er = 0$) for $R = 0.3$. The angle of the director orientation, θ (quiver angle) is given by $\theta = \frac{1}{2}\tan^{-1}(Q_{12}/Q_{11})$. The anchoring strength on the particle surface is varied from weak to strong. (a) $\log W = 0$, (b) $\log W = 0.8$, (c) $\log W = 1$ and (d) $\log W = 2$. The solid lines represent the director profiles (θ) and the background contour represent the magnitude of the order parameter S. Due to symmetry we show only half of the channel. The values of the relevant parameters used for the calculation are given in Table 1.

$0.1 < R < 0.3$ (Fig. 3d).

3.2. Static particle with fluid flow effects

Next, we include a flow field but hold the particle in place. We solve Eqs. (15), (16), (20), (21) subject to Eqs. (17)–(19), (22), (23) for the steady-state situation and $\partial \boldsymbol{Q}/\partial T = 0$ in Eqs. (20) and (21). This models a system with an obstacle (for example, a static micropillar [18]). On increasing the Ericksen number (while maintaining $Re \ll 1$) we observe three distinct regimes: weak, moderate and strong. The weak regime occurs for small Er. Here, the director profiles remain almost unchanged compared with those observed in the previous section with no flow field while the flow profile is significantly different to classical Poiseuille flow (Fig. 4a).

There are two stable director profiles, known as the horizontal (H) and vertical (V) states (Fig. 4d). The H and V states have different orientations at the channel centre (H-state, $\theta = 2n\pi$ and in V-state, $\theta = (n + 0.5)\pi$ where $n = 0, 1, 2, 3...$). In the H-state the directors splay, whereas in the V-state the director has a bent profile [44]. As the flow field is increased (through increasing Er) we enter the moderate flow regime (Fig. 4b),

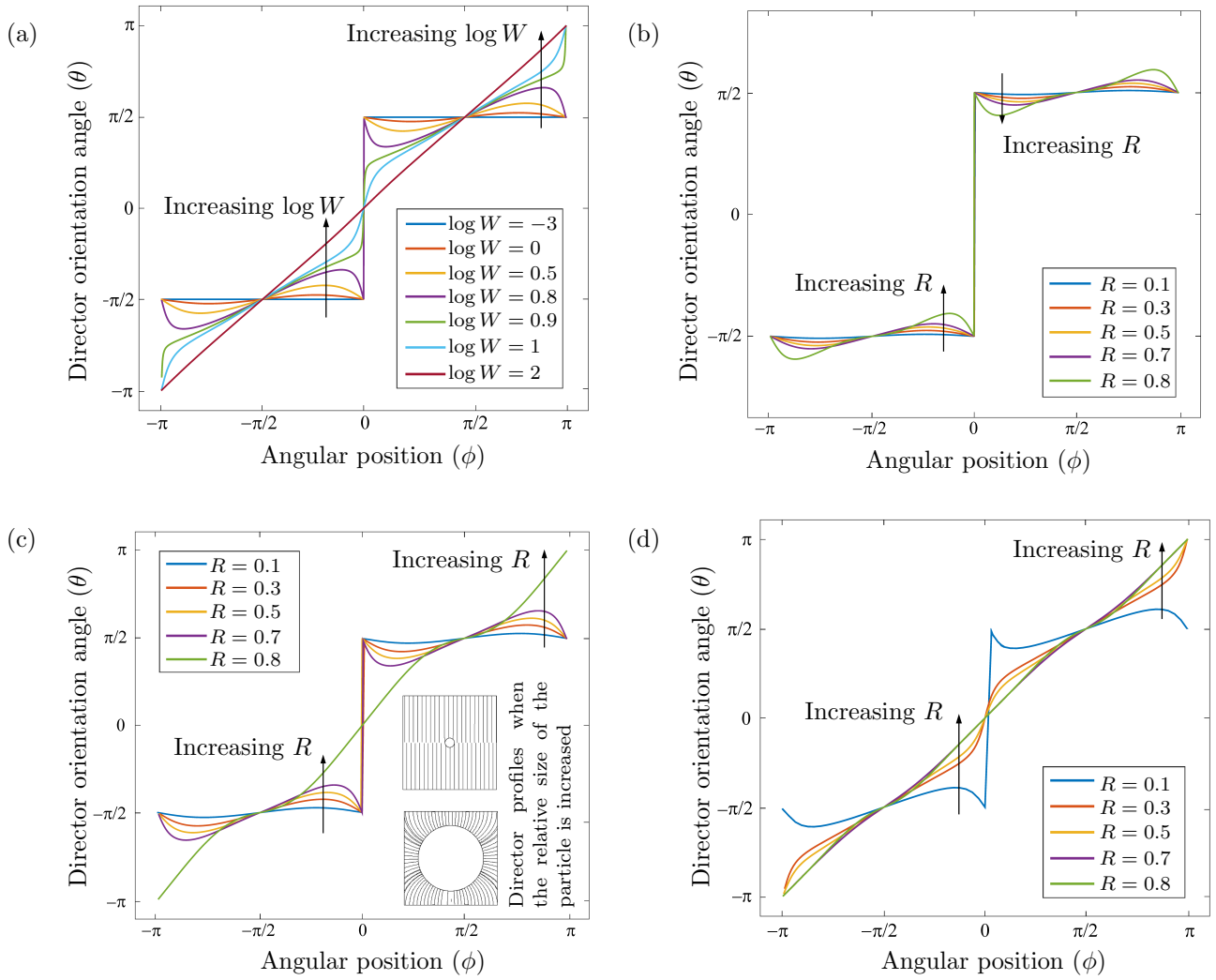

Figure 3: Variation of the director angle on the particle surface, with zero flow field ($Er = 0$) with different particle sizes and anchoring strength. In (a) the anchoring strength is increased with $\log W = -3, 0, 0.5, 0.8, 0.9, 1$ and 2 (in the direction of the arrow), for $R = 0.3$. In (b-d) the particle size is increased as $R = 0.1, 0.3, 0.5, 0.7$ and 0.8 (in the direction of the arrow) for (b) $\log W = 0$, (c) $\log W = 0.5$ (inset: qualitative visualization of the director orientation corresponding to $R = 0.1$ and 0.8), and (d) $\log W = 1$. Note that the particle is located at the centre of the channel with homeotropic boundary conditions on the surface. The values taken for all other parameters used for the calculation are given in Table 1.

one primarily observes the V-state and the flow begins to assume a parabolic profile (Fig. 4b).

As we further increase the flow rate (i.e., increase Er), the NLC stress weakens and we enter the strong regime (see Eqs. 15 and 16). The director field adapts to the more energetically favourable H-state configuration (Fig. 4c,d) and the flow assumes a fully developed Poiseuille profile. (Fig. 4c) [16]. This is consistent with the experimental observations of Sengupta et al. [2].

In Fig. 4e, we compare the location of the hyperbolic hedgehog defect on the leading side, as obtained from our numerical simulations, with the experimental results [18] for a channel with large aspect ratio, rendering the wall effect insignificant in the z-direction, consistent with our 2D set-up. We can see that the theoretical and experimental results are in close agreement for $Er < 100$. We also observe defects close to the particle body in the range $\pi/2 \leq \phi \leq \pi$, for moderate Er in agreement with the experiments in [13]. Further, the distance of the defect on the trailing side from the particle surface is roughly 0.17 times the diameter, in line with experiments that report this to be in the range of 0.05–0.25 times the diameter [13].

Of principal interest is the force experienced by a particle as a result of the viscous and elastic stresses exerted on the particle surface, given by Eq. (24), since this ultimately dictates the motion of the particle. Since the particle is placed at the channel centre, the overall lift force (F_y) is zero due to symmetry and the only force is in the x direction, F_x (drag). As we increase Er, the force on the particle increases, in the direction of the hydrodynamic pressure gradient (Fig. 5a).

When the anchoring strength ($\log W$ in Eq. 23) is increased, the driving force increases (Fig. 5b). This suggests that tuning the particle surface anchoring conditions by external stimuli, such as by photo-excitation [37] or an electric field [38] could assist in spatial reorganization in the nematohydrodynamic field.

While the viscous force on a particle due to hydrodynamic flow increases proportionally with particle radius [45], the effect of attractive normal boundary conditions on the channel walls is also felt as the particle size increases. These two forces act in competition, with the viscous forces attracting the particle to the centre and the wall forces drawing the particle towards the walls. As a result, a critical particle size exists for which the drag force is maximum ($R \approx 0.56$ for the parameters considered in Fig. 5c). For an isotropic

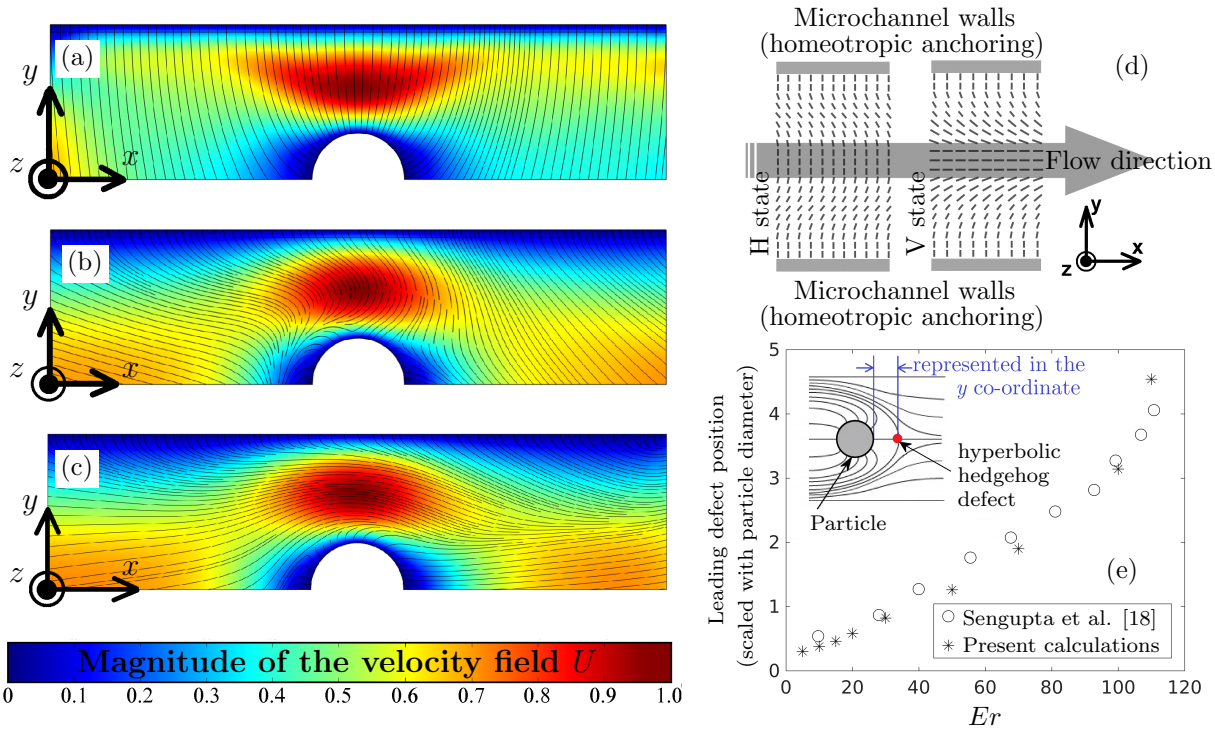

Figure 4: Profiles of the director orientation for (a) $Er = 0.001$ (weak flow), (b) $Er = 0.1$ (intermediate flow), (c) $Er = 10$ (strong flow). The solid black lines show the director orientation in the channel. The fluid flow is in the positive x direction. Due to symmetry we show only half of the channel. The background colour contour represents the axial velocity field U. Here $R = 0.3$. The bottom edge of the domain ($Y = 0$) is the symmetry condition. Homeotropic anchoring conditions are maintained on the channel walls as well as on the particle surface ($W \to \infty$). The values taken for all other parameters used for the calculation are given in Table 1. (d) Schematic representation of the V and H state configurations of the director alignment [16]. In (e) we show the location of the leading hyperbolic hedgehog defect comparing the experimental observations [18] for a flow past a static micropillar (for large aspect ratio, justifying the 2D setup) with the present calculations. The values used in this calculation are corresponding to the experimental conditions [18].

Newtonian fluid, the drag force continues to increases with particle size, purely due to the viscous stresses. On the other hand, the drag force in the NLC medium is sensitive to the value of Er, the particle size and $\log W$.

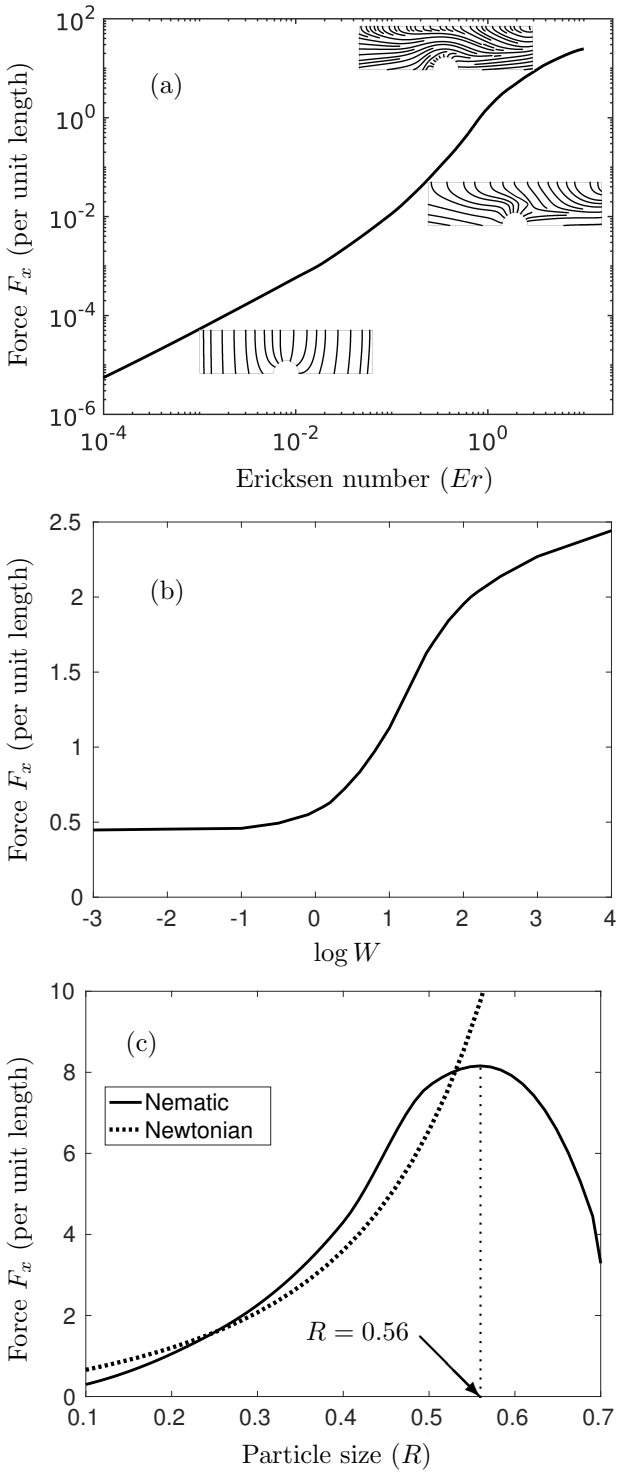

Figure 5: The axial force F_x on a static particle as a function of the (a) Ericksen number (Er) (the snapshot of the director orientation in the channel at different $Er = 0.001, 0.1, 10$ is shown as insets); (b) particle surface anchoring strength ($\log W$); and (c) particle size (R). The dotted line in (c) shows the force for an isotropic Newtonian fluid. The reference values of the parameters are $R = 0.3$, $Er = 1$ and $\log W = 3$. The values for all other parameters used for the calculation are given in Table 1.

3.3. Particle dynamics with fluid flow

3.3.1. Single particle

Having characterized the effect of placing a static particle in an NLC we now study the director profiles and particle trajectories when we allow the particle to move in response to the nematohydrodynamic field. We fix the Ericksen number ($Er = 0.02$) where the NLC elastic forces dominate over viscous forces [15, 13, 43] and solve the transient set of Eqs. (20)–(23) together with the flow hydrodynamics in Eqs. (10), (15)–(19). The particles are initially stationary ($\dot{X}_P = \dot{Y}_P = 0$) and released into the flow, and the initial condition for the NLC and the fluid flow is the equilibrium configuration for fixed particle position (as found in Section 3.2). We impose strong anchoring conditions on the particle surface. To compare this situation with a Newtonian fluid, we simply set the elastic constant, $\kappa = 0$ (thereby $Er \to \infty$).

For the Newtonian case, the cross-plane position $Y = 0$ is a stable equilibrium: if we release a particle from $Y \neq 0$ then the particle will evolve towards the centre as a result of the viscous stress exerted on the particle [46]. This behaviour is also observed for the values of the NLC parameters considered here, with the relaxation time approximately following an exponential decay to $Y = 0$ (Fig. 6a). As found in the previous section, the particle experiences two opposing forces: a viscous force, which acts to restore the particle towards the centre [46] and an attractive force between the strongly anchored channel wall and the particle surface [47], the latter of which is not present in a Newtonian fluid. The attractive force opposes the particle motion towards the centre, reducing the cross-stream velocity and increasing the time taken to reach the centre, compared with a Newtonian flow field (Fig. 6a,b).

Since there exists a competition between the NLC elastic stresses and the viscous forces on the colloidal particle, we hypothesize that there may be a critical vertical position for which the particle might migrate towards the wall instead of the centre. We analyse the lift force F_Y on the particle at $T = 0$ to determine whether it migrates towards the centre ($F_Y < 0$ since the particle is located at $Y > 0$ initially) or the wall ($F_Y > 0$). An unstable equilibrium is indeed found, at a critical vertical position, Y_P^*, for which the total lift force is zero (Fig. 6c). With increasing Er, the lift force approaches the limit of the Newtonian flow, where the particle always migrates towards the centre irrespective of its position. This suggests that, with a uniform particle distribution in the channel,

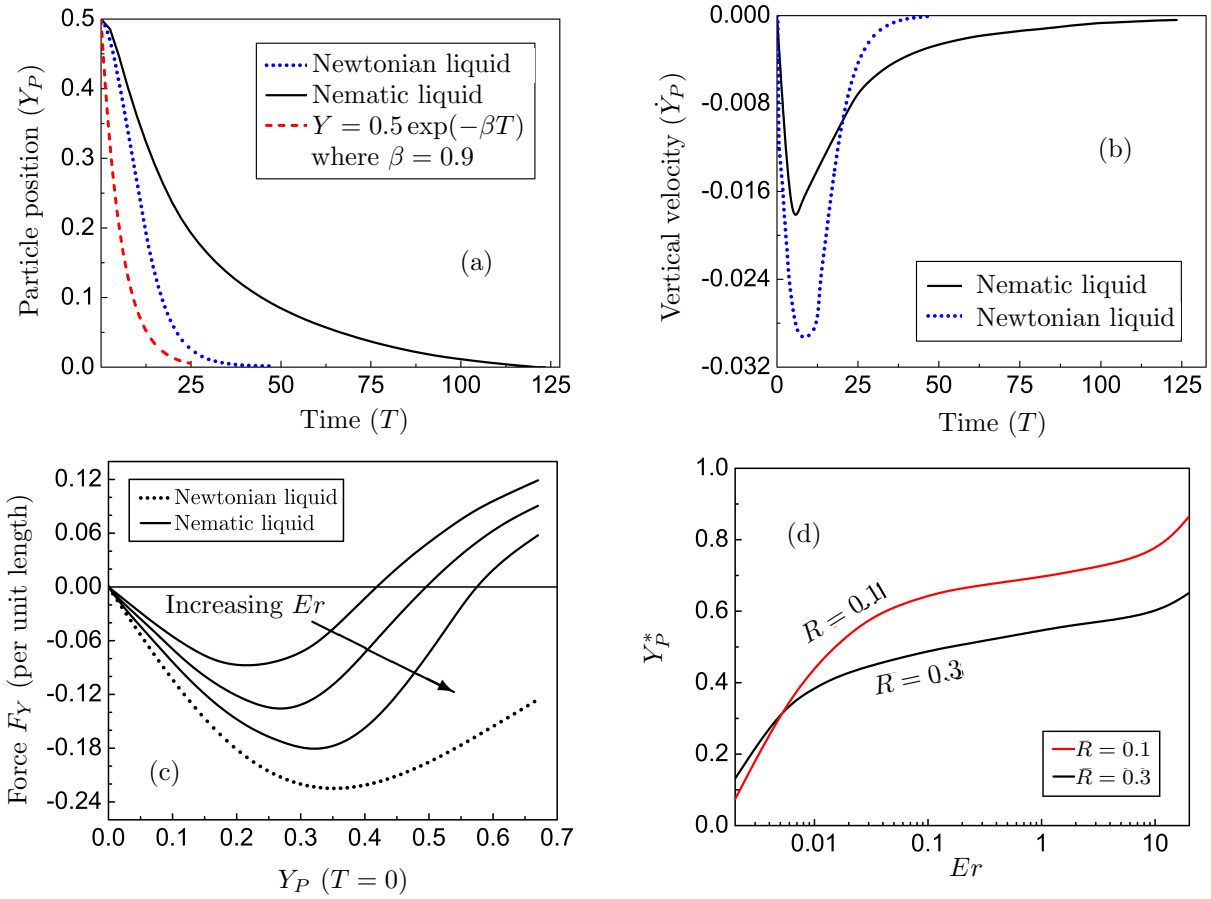

Figure 6: (a–b) Time evolution of a particle (black lines) that begins at position $Y = 0.5$ as it relaxes towards the centre $Y = 0$ in an NLC: (a) vertical coordinate of particle centre and (b) Y-component of the particle velocity. Here $R = 0.3$ and $Er = 0.02$. (c) The lift force (F_Y) experienced by the particle at different initial Y locations (of the particle centre) in the top half of the channel ($Y > 0$), for $R = 0.3$. The three solid curves are for nematic liquid with $Er = 0.02$, 0.2 and 2. The anchoring conditions on the particle and channel walls are homeotropic. If $F_Y < 0$ the particle migrates towards the centre. The dotted line is the behaviour of the particle in a viscous Newtonian flow, obtained by setting the elastic constant, $\kappa = 0$ leading to $Er \to \infty$. In the case of the Newtonian liquid the particle migrates towards the centre independent of its size [46]. (d) Variation of the critical Y position of the particle, Y_P^* (at $T = 0$ for which $F_Y = 0$) as a function of the Ericksen number for two different particle sizes. The values taken for all other parameters used for the calculation are given in Table 1. The anchoring conditions on the particle suraface and channel walls are homeotropic.

particles located on either side of the critical Y_P separate out, moving either towards the wall or towards the centre. This is somewhat similar to a Newtonian flow through a channel with porous walls, where the particles tend to flow towards the wall due to the transverse velocity induced by the suction (difference in pressure across the porous wall). However, all particles eventually deposit on (or penetrate) the wall in this case, while

for an NLC medium, a fraction of the introduced particles attach to the wall while the remainder move to the channel centre. The critical Y location is dependent on the size of the particle, anchoring strength and Ericksen number (Fig. 6d). With increasing particle size, the director interaction is stronger, yielding smaller values of Y_P^*, as observed from Fig. 6d.

3.3.2. Dual particle system

When two particles are released side by side (with zero initial velocities $\dot{X}_P = \dot{Y}_P = 0$ starting from $X = 0, Y = \pm 0.5$) within the microchannel, the attractive NLC forces between two homeotropically anchored particle surfaces results in significantly increased velocities in the Y direction, with the particles eventually touching one another (Fig. 7 and Fig. S2 in the Supplementary Information). The time evolution of the separation distance (see Fig. S2a) in the Supplementary Information) is qualitatively similar to the experimental observations in [10] for the case of the dominant elastic interactions ($Er \ll 1$). Upon agglomeration, the overall drag force is adjusted according to Fig. 5c. There are two stages in the dynamics: the first stage corresponds to the two isolated particles attracting each other and moving towards each other in a straight line ($T \lesssim 0.35$). In the second stage, the agglomerate reorients due to the quadrupolar interactions ($0.35 \lesssim T \lesssim 1.1$) (Fig. S2) [9, 3]. Due to the quadrupolar interactions [9, 3], the particles reorient themselves with the angle of inclination $\theta_p \approx 39^o$, with respect to the horizontal axis $Y = 0$ measured in the anti-clockwise direction. This is corroborated by Mondiot et al. [48] who find an angle of inclination $\theta_p = \sqrt{\arccos(4/7)} \approx 40.9°$, obtained by minimizing the quadrupolar interaction energy. This dual particle reorientation is driven by the minimum energy configuration state as described in [49]. The experimental observations in the literature support the attractive force in the direction of the quadrupolar interactions [47, 50, 51, 52]. The calculation of the Landau-de Gennes free energy of the two isolated particles suggests that the minimum energy depends on θ_p and the separation distance [47].

3.3.3. Triple-particle system

Finally, we consider the nematohydrodynamic effects on the mechanics of a triple-particle system in an NLC medium, for particle radii $R = 0.2$ (Fig. 8). In the first example, one particle is placed at the centre $X = Y = 0$ while the other two particles are at $X = -2, Y = \pm 0.5$. Initially all the particles are stationary ($\dot{X}_P = \dot{Y}_P = 0$ at $T = 0$). For $T \lesssim 0.1$ the two particles with initial position at $X = -2, Y = \pm 0.5$, aggregate before approaching the third (central) particle (Fig. 8a–c). When the two-particle agglomerate catches up with the single particle, the particles align themselves as an equiangular system (the centres form an equilateral triangle) to minimize the overall energy, due to the quadrupolar interactions (Fig. 8d). This is in close agreement with the experimental ob-

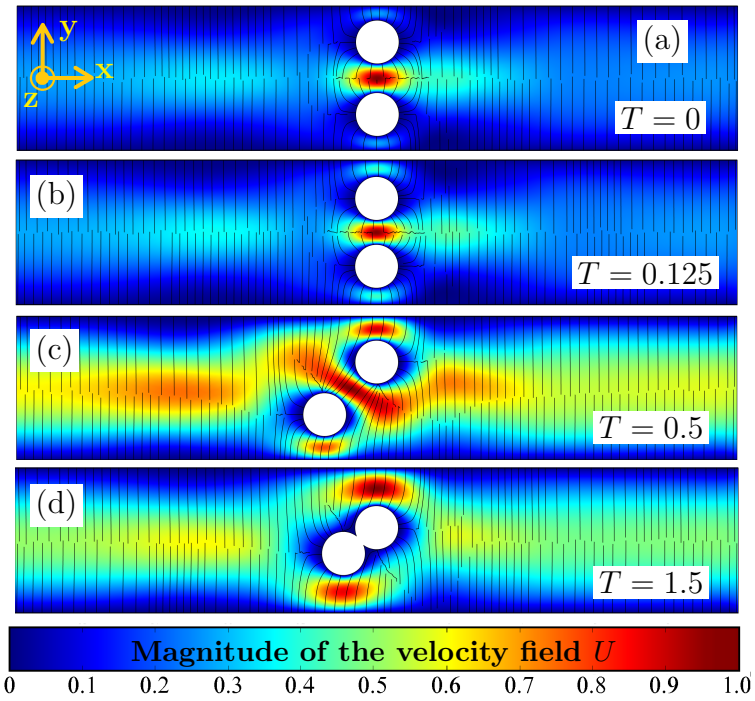

Figure 7: Snapshots showing the evolution with time of two particles placed in a microchannel located at $X = 0, Y = \pm 0.5$, as they approach each another and agglomerate: (a) $T = 0$; (b) $T = 0.125$; (c) $T = 0.5$; and (d) $T = 1.5$ (at which point the particles have reached their equilibrium configuration). Here $R = 0.3$ and $Er = 0.02$. The anchoring conditions on the particle and channel walls are homeotropic. The values taken for all other parameters used for the calculation are given in Table 1. The boundary conditions on the particle surfaces and channel walls are homeotropic. The fluid flow is in the positive x direction. The background colour contour represents the magnitude of the axial velocity field U.

servations for colloidal assemblies in a 2D NLC system, where the interparticle orientation angle in a triplet aggregate is found to be $56 \pm 1^\circ$ [7].

There are three distinct velocity zones in Fig. 8:

(i) For $T \lesssim 0.16$, the two off-centred particles approach one another while accelerating towards the third, central, particle. After these two particles aggregate, the overall drag in the X direction increases (as predicted by Fig. 5c), since the cumulative size of the dual-particle agglomerate is less than the critical size in Fig. 5c. The isolated central third particle is largely unaffected by the two particles during this part of the motion.

(ii) For $0.16 \lesssim T \lesssim 0.375$, the agglomerate approaches the isolated particle at a higher X-velocity than the central particle. Since the timescale of the final re-orientation of the dual-particle system (due to the quadrupolar interactions) is longer ($T \geq 1$ as seen in Fig. S2a), the two-particle globule catches up with the central particle before the transitional reorientation can occur as observed in the dual-particle system.

(iii) For $T \gtrsim 0.375$, the three particles attach to each other to form a triple agglomerate that moves as a whole. We note that a triplet formed of individual particles (of size R) has an effective size of $(1+\sqrt{3})R \approx 0.54$ (for $R = 0.2$), which is below the critical size that maximizes the drag, $R_{max} = 0.56$ in Fig. 5c. This results in an increased velocity due to the enhanced drag as observed in Fig. 5c.

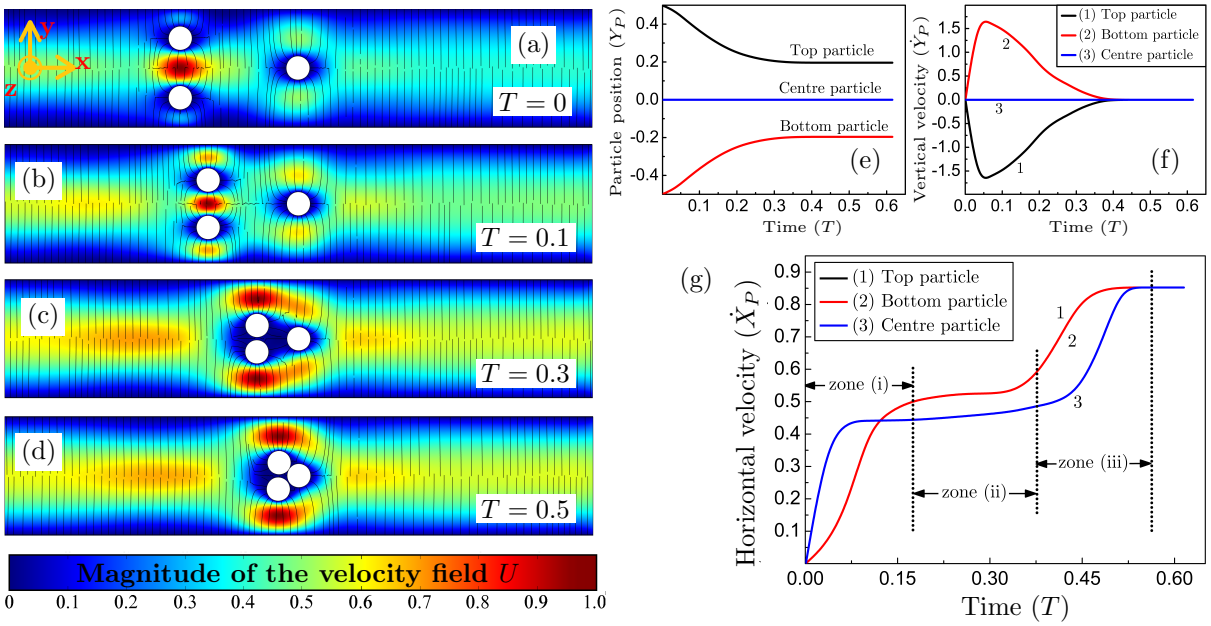

Figure 8: (a–d) Snapshots showing the evolution with time of three particles placed in a microchannel located at $X = -0.2$, $Y = \pm 0.5$ and $X = 0$, $Y = 0$, relaxing towards the equilibrium: (a) $T = 0$; (b) $T = 0.1$; (c) $T = 0.3$; and (d) $T = 0.5$ (at which point the three-particle system has reached equilibrium). The fluid flow is in the positive x direction. The background colour contour represents the magnitude of the axial velocity field U. (e–g) Trajectory information of the triplet system; (e) vertical coordinates of particle centres; (f) Y-components of the particle velocities and (g) X-components of the particle velocities. Here $R = 0.2$ and $Er = 0.02$. The anchoring conditions on the particle and channel walls are strongly homeotropic. All other parameters used for the calculation are given in Table 1. The boundary conditions on the particle surfaces and channel walls are homeotropic.

The initial configuration plays a key role in the subsequent dynamics of the triplet agglomeration. For a zig-zag combination of three particles with initially large interparticle separation distance there is an intermediate linear configuration of three particles (see Fig. 9). The intermediate system persists for a long time ($T = 0.5 - 2.7$), which suggests that the linear state is relatively stable. The subsequent behaviour is then equivalent to the behaviour of an initial condition of three linearly placed particles. The final configuration is always found to be equiangular irrespective of the initial configuration (triangular, zig-zag or linear) or the interparticle separation distance (see Fig. 9a, b). However, the

orientation of the triangular agglomerate does depend on the initial state (Figs. 8d, 9a,b).

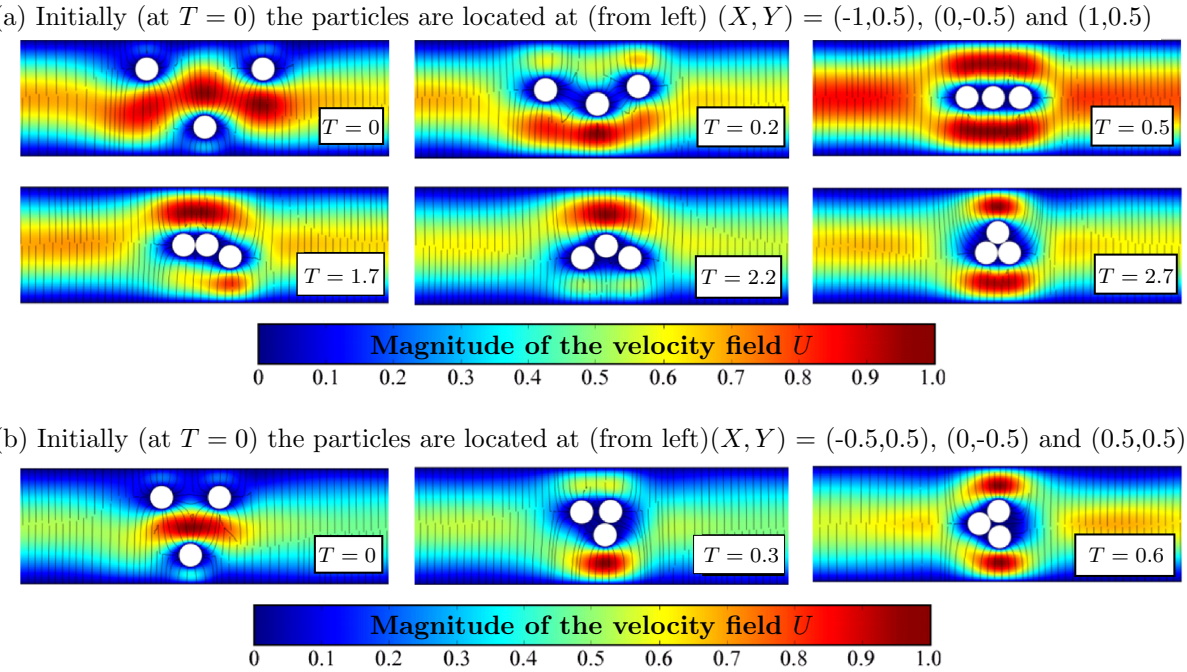

Figure 9: Snapshots showing the time evolution of the triplet arranged initially in a zig-zag configuration, for an interparticle separation distance of (a) 5 particle radii; and (b) 2.5 particle radii. Here $R = 0.2$ and $Er = 0.02$. The anchoring conditions on the particle and channel walls are strongly homeotropic. All other parameter values used for the calculation are given in Table 1. The fluid flow is in the positive x direction. The background colour contour represents the magnitude of the axial velocity field U.

For large values of Er, the system is highly nonlinear and more topological defects are expected. Our results are valid for $Er < 1$; for $Er > 1$, the particle self-assembly is influenced by the topological defects [5]. For $Re \ll 1$ and $Er \gtrsim 200$, unexpected phenomena such as cavitation around the particle has been observed [53].

4. Conclusions

In this paper we use a continuum Beris–Edwards framework to simulate the motion of particles immersed in an NLC microfluidic channel, motivated by recent experimental work. We first consider the response of the NLC director field when a particle is placed in the channel in the absence of a flow.

The director orientation around the particle depends on the particle surface anchoring and the relative particle size. The system properties also depend on the Ericksen number, Er, which measures the relative effect of the viscous to NLC elastic forces. As the Ericksen

number is increased, the hyperbolic hedgehog defect on the leading and trailing side of the particle moves further away from the particle surface, an observation that is supported by experiments [18]. The particle experiences forces due to the viscous drag and due to the interaction between the homeotropic anchored particle surfaces and channel walls. As the particle increases in size, the viscous the NLC elastic forces oppose each other and the drag force is maximum for a critical particle size. There is also a critical particle location that determines particle separation i.e. particles on either side of this critical location either migrate towards the channel walls or towards the channel centre. This gives us a potential mechanism for sorting a suspension of particles of different size, without the need for any manual separation, which is impossible in an isotropic fluid.

We then consider a dual-particle system, and find that the particles align at an angle of around 39° relative to the walls, which is close to the experimentally reported value of 41° [48]. When a third particle is added to the system, the particles form an equiangular triplet agglomerate, in agreement with experimental observations [10]. While the final particle arrangement appears to be independent of the initial configuration, the evolution towards this final state is sensitive to the initial state, and in some instances one can obtain interim locally stable configurations. For example, a set-up of linearly aligned particles appears to be locally stable.

We illustrate a variety of physical phenomena that are not observed in isotropic fluids. Our numerical analysis demonstrates the rich hydrodynamic landscape for NLC microfluidics and how the coupling between flow, anchoring, particle sizes and NLC order can be tuned to control the mechanisms of particle migration, self-reorganization and separation. We hope that our work will inspire future experimental study into particle separation and self-assembly mechanisms.

Acknowledgements

The authors gratefully acknowledge helpful discussions with L. J. Cummings and D. Vigolo. AM and IMG are grateful for discussions on nematic microfluidics with A. Sengupta and for the UK Fluids Network Short Research Visit scheme for facilitating their collaboration. SM is grateful to EPSRC and the Royal Society for financial support. AM's research is supported by an EPSRC Career Acceleration Fellowship EP/J001686/1 and EP/J001686/2, an OCIAM Visiting Fellowship and the Advanced Studies Centre at Ke-

ble College. IMG gratefully acknowledges support from the Royal Society through a University Research Fellowship.

References

[1] J. P. F. Lagerwall and G. Scalia. A new era for liquid crystal research: Applications of liquid crystals in soft matter nano-, bio-and microtechnology. *Current Applied Physics*, 12(6):1387–1412, 2012.

[2] A. Sengupta, U. Tkalec, M. Ravnik, J. M. Yeomans, C. Bahr, and S. Herminghaus. Liquid crystal microfluidics for tunable flow shaping. *Phys. Rev. Lett.*, 110:048303, Jan 2013.

[3] O. D. Lavrentovich. Transport of particles in liquid crystals. *Soft Matter*, 10:1264–1283, 2014.

[4] I.-H. Lin, G. M. Koenig Jr, J. J. de Pablo, and N. L. Abbott. Ordering of solid microparticles at liquid crystal–water interfaces. *J. Phys. Chem. B*, 112(51):16552–16558, 2008.

[5] A. Sengupta, C. Bahr, and S. Herminghaus. Topological microfluidics for flexible micro-cargo concepts. *Soft Matter*, 9(30):7251–7260, 2013.

[6] M. Škarabot, M. Ravnik, S. Žumer, U. Tkalec, I. Poberaj, D. Babič, N. Osterman, and I. Muševič. Interactions of quadrupolar nematic colloids. *Phys. Rev. E*, 77(3):031705, 2008.

[7] I. Muševič, M. Škarabot, U. Tkalec, M. Ravnik, and S. Žumer. Two-dimensional nematic colloidal crystals self-assembled by topological defects. *Science*, 313(5789):954–958, 2006.

[8] J. C. Loudet, P. Hanusse, and P. Poulin. Stokes drag on a sphere in a nematic liquid crystal. *Science*, 306(5701):1525–1525, 2004.

[9] T. Turiv, I. Lazo, A. Brodin, B. I. Lev, V. Reiffenrath, V. G. Nazarenko, and O. D. Lavrentovich. Effect of collective molecular reorientations on brownian motion of colloids in nematic liquid crystal. *Science*, 342(6164):1351–1354, 2013.

[10] P. Poulin, H. Stark, T. C. Lubensky, and D. A. Weitz. Novel colloidal interactions in anisotropic fluids. *Science*, 275(5307):1770–1773, 1997.

[11] B. Senyuk, D. Glugla, and I. I. Smalyukh. Rotational and translational diffusion of anisotropic gold nanoparticles in liquid crystals controlled by varying surface anchoring. *Physical Review E*, 88(6):062507, 2013.

[12] S. D. Peroukidis and S. H. L. Klapp. Spontaneous ordering of magnetic particles in liquid crystals: From chains to biaxial lamellae. *Phys. Rev. E*, 92:010501, Jul 2015.

[13] J.-I. Fukuda, H. Stark, M. Yoneya, and H. Yokoyama. Dynamics of a nematic liquid crystal around a spherical particle. *J. Phys.: Condensed Matter*, 16(19):S1957, 2004.

[14] O. V. Kuksenok, R. W. Ruhwandl, S. V. Shiyanovskii, and E. M. Terentjev. Director structure around a colloid particle suspended in a nematic liquid crystal. *Phys. Rev. E*, 54(5):5198, 1996.

[15] R. W. Ruhwandl and E. M. Terentjev. Friction drag on a cylinder moving in a nematic liquid crystal. *Zeitschrift für Naturforschung A*, 50(11):1023–1030, 1995.

[16] S. A. Jewell, S. L. Cornford, F. Yang, P. S. Cann, and J. R. Sambles. Flow-driven transition and associated velocity profiles in a nematic liquid-crystal cell. *Phys. Rev. E*, 80(4):041706, 2009.

[17] G. Tóth, C. Denniston, and J. M. Yeomans. Hydrodynamics of topological defects in nematic liquid crystals. *Phys. Rev. Lett.*, 88(10):105504, 2002.

[18] A. Sengupta, C. Pieper, J. Enderlein, C. Bahr, and S. Herminghaus. Flow of a nematogen past a cylindrical micro-pillar. *Soft Matter*, 9(6):1937–1946, 2013.

[19] L. Giomi, L. Mahadevan, B. Chakraborty, and M. F. Hagan. Banding, excitability and chaos in active nematic suspensions. *Nonlinearity*, 25(8):2245, 2012.

[20] M. Crespo, A. Majumdar, A. M. Ramos, and I. M. Griffiths. Solution landscapes in nematic microfluidics. *Physica D: Nonlinear Phenomena*, 351:1–13, 2017.

[21] T. G. Anderson, E. Mema, L. Kondic, and L. J. Cummings. Transitions in Poiseuille flow of nematic liquid crystal. *Int. J. Non-Linear Mech.*, 75:15–21, 2015.

[22] A. Sengupta. Topological microfluidics: present and prospects. *Liquid Crystals Today*, 24(3):70–80, 2015.

[23] A. Sengupta. *Nematic Liquid Crystals Confined Within a Microfluidic Device: Static Case*, pages 72–76. Springer International Publishing, 2013.

[24] G.-Q. Chen, A. Majumdar, D. Wang, and R. Zhang. Global existence and regularity of solutions for active liquid crystals. *J. Diff. Eq.*, 263(1):202–239, 2017.

[25] D. Marenduzzo, E. Orlandini, and J. M. Yeomans. Hydrodynamics and rheology of active liquid crystals: A numerical investigation. *Phys. Rev. Lett.*, 98(11):118102, 2007.

[26] A. M. Sonnet, P. L. Maffettone, and E. G. Virga. Continuum theory for nematic liquid crystals with tensorial order. *J. Non-Newtonian Fluid Mechanics*, 119(1):51–59, 2004.

[27] P. G. De Gennes. Short range order effects in the isotropic phase of nematics and cholesterics. *Molecular Crystals and Liquid Crystals*, 12(3):193–214, 1971.

[28] M. E. Cates, O. Henrich, D. Marenduzzo, and K. Stratford. Lattice Boltzmann simulations of liquid crystalline fluids: active gels and blue phases. *Soft Matter*, 5(20):3791–3800, 2009.

[29] T. B. Liverpool and M. C. Marchetti. Rheology of active filament solutions. *Phys. Rev. Lett.*, 97(26):268101, 2006.

[30] A. N. Beris and B. J. Edwards. *Thermodynamics of Flowing Systems: with Internal Microstructure*. Oxford Engineering Science Series. Oxford University Press, 1994.

[31] J. Happel and H. Brenner. *Low Reynolds number hydrodynamics: with special applications to particulate media*, volume 1. Springer Science & Business Media, 2012.

[32] H. Stark, D. Ventzki, and M. Reichert. Recent developments in the field of colloidal dispersions in nematic liquid crystals: the stokes drag. *J. Phys.: Condensed Matter*, 15(1):S191, 2002.

[33] H. Stark and D. Ventzki. Stokes drag of spherical particles in a nematic environment at low Ericksen numbers. *Phys. Rev. E*, 64(3):031711, 2001.

[34] R. W. Pryor. *Multiphysics modeling using COMSOL: a first principles approach*. Jones & Bartlett Publishers, 2009.

[35] Lev Mikhaĭlovich Blinov and Vladimir Chigrinov. *Electrooptic effects in liquid crystal materials*. Springer Science & Business Media, 2012.

[36] C. Luo, A. Majumdar, and R. Erban. Multistability in planar liquid crystal wells. *Phys. Rev. E*, 85(6):061702, 2012.

[37] T. Ikeda. Photomodulation of liquid crystal orientations for photonic applications. *J. Mater. Chem.*, 13:2037–2057, 2003.

[38] H. J. Deuling. Deformation of nematic liquid crystals in an electric field. *Molecular Crystals and Liquid Crystals*, 19(2):123–131, 1972.

[39] M. Schadt and W. Helfrich. Voltage-dependent optical activity of a twisted nematic liquid crystal. *Appl. Physics Lett.*, 18(4):127–128, 1971.

[40] B. Jerome. Surface effects and anchoring in liquid crystals. *Reports on Progress in Physics*, 54(3):391, 1991.

[41] J. Fukuda and H. Yokoyama. Stability of the director profile of a nematic liquid crystal around a spherical particle under an external field. *Eur. Phys. J. E*, 21(4):341–347, 2006.

[42] R. W. Ruhwandl and E. M. Terentjev. Monte Carlo simulation of topological defects in the nematic liquid crystal matrix around a spherical colloid particle. *Phys. Rev. E*, 56(5):5561, 1997.

[43] A. Sengupta, S. Herminghaus, and B. Bahr. Liquid crystal microfluidics: surface, elastic and viscous interactions at microscales. *Liquid Crystals Reviews*, 2(2):73–110, 2014.

[44] M. J. Towler, E. J. Acosta, H. G. Walton, C. Tombling, M. D. Tillin, B. Henley, E. J. Walton, T. Kawamura, A. Fujii, and Y. Yamada. Liquid crystal display device. *US Patent 6,714,276*, 2004.

[45] L. G. Leal. *Advanced transport phenomena: fluid mechanics and convective transport processes*. Cambridge University Press, 2007.

[46] B. H. Yang, J. Wang, D. D. Joseph, H. H. Hu, T.-W. Pan, and R. Glowinski. Migration of a sphere in tube flow. *J. Fluid Mech.*, 540:109–131, 2005.

[47] M. Tasinkevych and D. Andrienko. Colloidal particles in liquid crystal films and at interfaces. *Condensed Matter Phys.*, 13(3):1–20, 2010.

[48] F. Mondiot, R. Botet, P. Snabre, O. Mondain-Monval, and J.-C. Loudet. Colloidal aggregation and dynamics in anisotropic fluids. *Proc. Nat. Academy Sciences*, 111(16):5831–5836, 2014.

[49] B. Senyuk, O. Puls, M. Tovkach, S. B. Chernyshuk, and I. I. Smalyukh. Hexadecapolar colloids. *Nature Comm.*, 7, 2016.

[50] M. S. Al-Barwani, G. S. Sutcliffe, and M. P. Allen. Forces between two colloidal particles in a nematic solvent. *J. Phys. Chem. B*, 108(21):6663–6666, 2004.

[51] K. Takahashi, M. Ichikawa, and Y. Kimura. Direct measurement of force between colloidal particles in a nematic liquid crystal. *J. Phys.: Condensed Matter*, 20(7):075106, 2008.

[52] K. Takahashi, M. Ichikawa, and Y. Kimura. Force between colloidal particles in a nematic liquid crystal studied by optical tweezers. *Phys. Rev. E*, 77(2):020703, 2008.

[53] T. Stieger, H. Agha, M. Schoen, M. G. Mazza, and A. Sengupta. Hydrodynamic cavitation in Stokes flow of anisotropic fluids. *Nature Communications*, 8, 2017.